High Pressure Raman Spectroscopy and X-ray Diffraction of $K_2Ca(CO_3)_2$ Bütschliite: Multiple Pressure-Induced Phase Transitions in a Double Carbonate

Authors:
G. Zeff[1,*]
B. Kalkan[1,2]
K. Armstrong[1,2]
M. Kunz[2]
Q. Williams[1]

[1] Department of Earth and Planetary Sciences, University of California, Santa Cruz, CA 95064 USA
[2] Advanced Light Source, Lawrence Berkeley National Laboratory, Berkeley, CA 94720, USA
[*]Corresponding author: gzeff@ucsc.edu

Keywords: Carbonate, high-pressure, Raman spectroscopy, x-ray diffraction

Acknowledgements: This work was supported by the US National Science Foundation through award EAR-2017294. This research used resources of the Advanced Light Source (beamline 12.2.2) at Lawrence Berkeley National Laboratory, which is DOE Office of Science User facility under Contract No. DE-AC02-05CH11231. This research was partially supported by COMPRES, the Consortium for Materials Properties Research in Earth Sciences under NSF Cooperative Agreement EAR 1606856, and SEES, Synchrotron Earth and Environmental Science under NSF Cooperative Agreement EAR 2223273.

Abstract

The crystal structure and bonding environment of $K_2Ca(CO_3)_2$ bütschliite were probed under isothermal compression via Raman spectroscopy to 95 GPa and single crystal and powder x-ray diffraction to 12 and 68 GPa, respectively. A second order Birch-Murnaghan equation of state fit to the x-ray data yields a bulk modulus, $K_0 = 46.9$ GPa with an imposed value of $K_0' = 4$ for the ambient pressure-phase. Compression of bütschliite is highly anisotropic, with contraction along

31 the *c*-axis accounting for most of the volume change. Bütschliite undergoes a phase transition to
32 a monoclinic *C*2/*m* structure at around 6 GPa, mirroring polymorphism within isostructural
33 borates. A fit to the compression data of the monoclinic phase yields $V_0 = 322.2$ Å^3, $K_0 = 24.8$
34 GPa and $K_0' = 4.0$ using a 3rd order fit; the ability to access different compression mechanisms
35 gives rise to a more compressible material than the low-pressure phase. In particular,
36 compression of the *C*2/*m* phase involves interlayer displacement and twisting of the [CO_3] units,
37 and an increase in coordination number of the K^+ ion. Three more phase transitions, at ~28, 34,
38 and 37 GPa occur based on the Raman spectra and powder diffraction data: these give rise to
39 new [CO_3] bonding environments within the structure.

1. Introduction

The rare carbonate mineral bütschliite (also spelled buetschliite), with chemical formula $K_2Ca(CO_3)_2$, has been observed to form in highly disparate geological environments. First discovered and named in 1947, the mineral was initially found in wood-ash stones from the western United States (Milton and Axelrod 1947). More recently, bütschliite has been identified as an inclusion/daughter phase in mantle-derived olivine and diamond crystals (Abersteiner et al. 2022; Logvinova et al. 2019). Occurrences of bütschliite in granitic pegmatites have also been reported (Bermanec et al. 2011).

The identification of bütschliite inclusions not only in diamond, but in mantle-derived olivine as well, suggests that alkaline carbonate melts and solid mineral phases could play an important role in the petrogenesis of kimberlites and carbonatites. Indeed, Chayka et al. (2021) suggests that even alkaline-poor carbonatites may be derived from substantially alkaline-enriched parental magmas. Candidates for potassium-bearing mineral phases in the mantle are limited: the phyllosilicate mineral phlogopite and the amphibole richterite have been identified in a number of mantle-derived xenoliths and within the results of experiments on hydrated and carbonated peridotite (e.g., Harlow and Davies, 2004; Meltzer and Kessler, 2023), but in terms of potassic carbonate minerals, only bütschliite has been reported in mantle assemblages. Several studies have explored the stability of the related synthetic material $K_2Mg(CO_3)_2$ (Brey et al. 2011; Golubkova et al. 2015; Arefiev et al. 2018), but this compound has not been identified as a mineral phase in nature.

Investigations into the stability and structure of bütschliite at non-ambient conditions have been limited. McKie (1990) studied the system $K_2Ca(CO_3)_2$-$Na_2Mg(CO_3)_2$ and determined that fairchildite, the intrinsically-disordered high-temperature polymorph of bütschliite, and

eitelite ($Na_2Mg(CO_3)_2$) can form an extensive solid solution, while bütchsliite and eitelite are almost completely immiscible (limited to < 2 mol% solid solution). Arefiev et al. (2019) and Shatskiy et al. (2015) studied the K_2CO_3-$CaCO_3$ system at high temperatures and 3 and 6 GPa, respectively, and observed the presence of bütschliite as a sub-solidus phase at each pressure. Hou et al. (2022) and Tian et al. (2023) employed first-principles simulations via the VASP calculational package (Kresse and Furthmüller, 1996) to examine the structure of bütschliite under isothermal compression to ~22 and ~26 GPa, respectively, and both studies calculated transitions to monoclinic and triclinic phases, albeit with different sequences and at different pressures. Zhuravlev (2022) deployed the CRYSTAL17 *ab initio* package to calculate the elastic constants of bütschliite under compression. He noted that the C_{44} shear elastic constant appeared to be soft, trending towards zero at 5.8 GPa, thus indicating that an unspecified phase transition is anticipated at this pressure. In this study, we present the results of the first in-situ high-pressure, ambient-temperature Raman spectroscopy and synchrotron x-ray diffraction experiments on bütschliite to 95 GPa. These delineate the transition pressures and properties of the high-pressure phases of this material. Our results shed light on the crystal structures and bonding environments of low symmetry carbonate minerals at high pressures, as well as the role played by cations in the compressibilities of these minerals.

2. Methods and Sample Synthesis

Bütschliite crystals were synthesized following the method of Pabst (1974), in which millimeter-scale cleavage rhombs of optical-quality calcite are immersed in a saturated K_2CO_3 solution and heated to between 50 to 70°C for several days. Crystals grown in this manner are typically euhedral and free of inclusions, making them suitable for both optical and x-ray-based

measurements. While bütschliite was the most abundant phase produced by this method, small amounts of other (possibly hydrated) potassium/calcium carbonate phases were sporadically detected in Raman spectroscopy measurements. Bütschliite is hygroscopic and deliquesces readily in air over the course of a few hours. Samples were stored in toluene after synthesis; crystals stored in this organic liquid remain stable indefinitely. As a mildly non-hydrostatic pressure medium, silicone oil was chosen for some experiments over a methanol/ethanol solution to minimize the risk of crystal degradation due to hydration; neon, which more closely approaches hydrostaticity at high pressures, was used as a pressure medium for a large number of the experiments. Notably, crystals stored in high purity methanol/ethanol solutions (< 0.01% water) at slightly elevated pressure did not show any signs of degradation over the course of a few weeks.

2.1 Raman Spectroscopy

Ambient and high-pressure Raman spectra were collected on a LabRAM HR Evolution spectrometer equipped with a 532 nm excitation laser nominally rated at 50 mW. A grating of 1200 lines/mm was employed and spectral resolution is ~1 cm^{-1}. Samples were loaded into symmetric-style diamond anvil cells equipped with 250 or 350 μm culet diamonds. Rhenium gaskets were used for all Raman experiments, and silicone oil or neon were used as pressure transmitting media in different runs. Ruby spheres or small amounts of ruby powder were loaded into the sample chamber and the calibration of Shen et al. (2020) was used for pressure determination. Ruby emission lines became unresolvable at pressures above ~85 GPa, and pressures were determined from the Raman shift of the diamond anvil measured at the center of

the culet (Akahama and Kawamura, 2006). Peak fitting and deconvolution were carried out with the Horiba LabSpec 6 software.

2.2 Synchrotron Single Crystal X-ray Diffraction

The high-pressure single-crystal x-ray diffraction experiments were performed at ambient temperature using short symmetric, Merrill-Bassett, and BX-90 diamond anvil cells equipped with 300–400 μm culet Boehler-Almax diamond anvils and c-BN/WC seats providing a ~90° opening angle. Re and Inconel gaskets were indented to ~30–50 μm, and sample chambers were drilled with diameters of 150–180 μm with a laser-milling system. Single-crystal samples, measuring ~50×50×10 μm^3, were mounted directly onto the diamond culet with a small amount of vacuum grease to minimize movement of the crystal during loading of the pressure media. Neon or silicone oil were used as pressure transmitting media in different runs. Pressure media were loaded into the sample chambers immediately after sample loading to avoid the risk of sample degradation.

The high-pressure diffraction data were collected at end-station 2 of beamline 12.2.2 of the Advanced Light Source at Lawrence Berkeley National Laboratory using synchrotron x-rays monochromated by silicon (111) with an energy of 30 keV ($\lambda = 0.4132(1)$ Å), focused to a 10×10 μm^2 spot. The diffraction spots were collected on a Pilatus3 S 1M fast detector. Exposure times ranged from 1 to 8 sec/º. Detector distance and wavelength calibration were performed using CeO_2 powder and a NIST single-crystal ruby sphere. The sample was aligned to the rotational center of the goniometer, and data were collected throughout the range of $\theta = -35°$ to 35° (in 0.50° and 1.00° increments) for a total coverage of ~70° sample rotation. The diffraction data were corrected for the reduction of reflection intensities due to the DAC-gasket shadowing

and indexed and reduced to *hkl* sorted structure factors by integration using the program SAINT v8.34A in APEX3 (Bruker, 2016). Before structure solution steps, a few individual reflections (with negative and almost zero intensities) were removed from the data set because their intensities were affected by simultaneous diffraction events in the diamond anvils. A total of ~150–250 unique reflections were available for subsequent structural analysis. The structure solutions were carried out with SHELXS (embedded in APEX) using direct methods and refined with SHELXT (Sheldrick, 2008) by full-matrix least-squares on F^2. For every structure, ~34 parameters including overall scale factor, isotropic atomic displacement factors, and fractional coordinates of the atoms were refined; for bütschliite-II, the greater number of distinguishable atoms within the unit cell increased the number of parameters solved. Ball and stick structural models were produced in *VESTA 3* (Momma and Izumi, 2011).

2.3 Synchrotron Powder X-ray Diffraction

High-pressure powder x-ray diffraction measurements were also collected at ALS beamline 12.2.2, using BX-90, symmetric, and Merrill-Bassett diamond anvil cells with diamond culet sizes ranging between 300–500 μm. Diamonds were mounted on c-BN or WC seats. Inconel and rhenium foils were used for gasket materials, and silicone oil or neon were employed as pressure media in different runs. An exposure time of 30 sec was used and x-ray beam energies of 25 and 30 keV were used in different runs. Powder patterns were indexed with the LeBail method in GSAS-II (Toby and Von Dreele, 2013). Peterson (2004) suggests that the LeBail method can be inappropriate for low symmetry phases; however, this method was preferable to the Rietveld method for these samples since the acquired powder patterns were highly textured due to apparent preferred orientation of grains of the first high pressure phase.

3. Results and Discussion

3.1 Single Crystal and Powder X-ray Diffraction of Bütschliite

X-ray diffraction measurements were previously made on bütschliite-I under ambient conditions. Mrose et al. (1966) erroneously reported, due to a misprint in the original publication, that bütschliite crystallizes in the $R\bar{3}$ space group. Pabst (1974) determined that bütschliite crystallizes in the $R\bar{3}m$ space group (reported as $R\bar{3}2/3$) with a = 5.38 Å, c = 18.12 Å, and Z = 3, and has a structure very similar to that of eitelite, despite the difference in space groups (eitelite belongs to the $R\bar{3}$ space group and lacks a mirror plane due to rotation of the carbonate anions). The ambient bütschliite structure is characterized by planar sheets of [CO_3] units separated by alternating interstitial layers of Ca^{2+} and K^+ cations (Figure 1a,b). Pabst (1974) reports a unit cell volume of 454.2 $Å^3$, which is in excellent agreement with our measured value of 453.9 $Å^3$. Compression of bütschliite is strongly anisotropic, with contraction of the c-axis accounting for most of the volume change (Figure 2a–c). The contraction of the unit cell along the c-axis follows a steeply linear trend up to the first phase transition, with $\Delta c/\Delta P$ = 0.23 Å/GPa. This style of anisotropy has also been observed in the isostructural synthetic compound $K_2Mg(CO_3)_2$, and is a result of the greater compressibility of the [KO_9] polyhedra compared to the alkaline earth cation polyhedra and trigonal planar [CO_3] units (Golubkova et al., 2015). Most of the reduction in the bütschliite unit cell volume occurs via reductions of the K-Ca and K-O distances. The C-O, O-O, and Ca-O distances remain largely unchanged during compression (Figure 1).

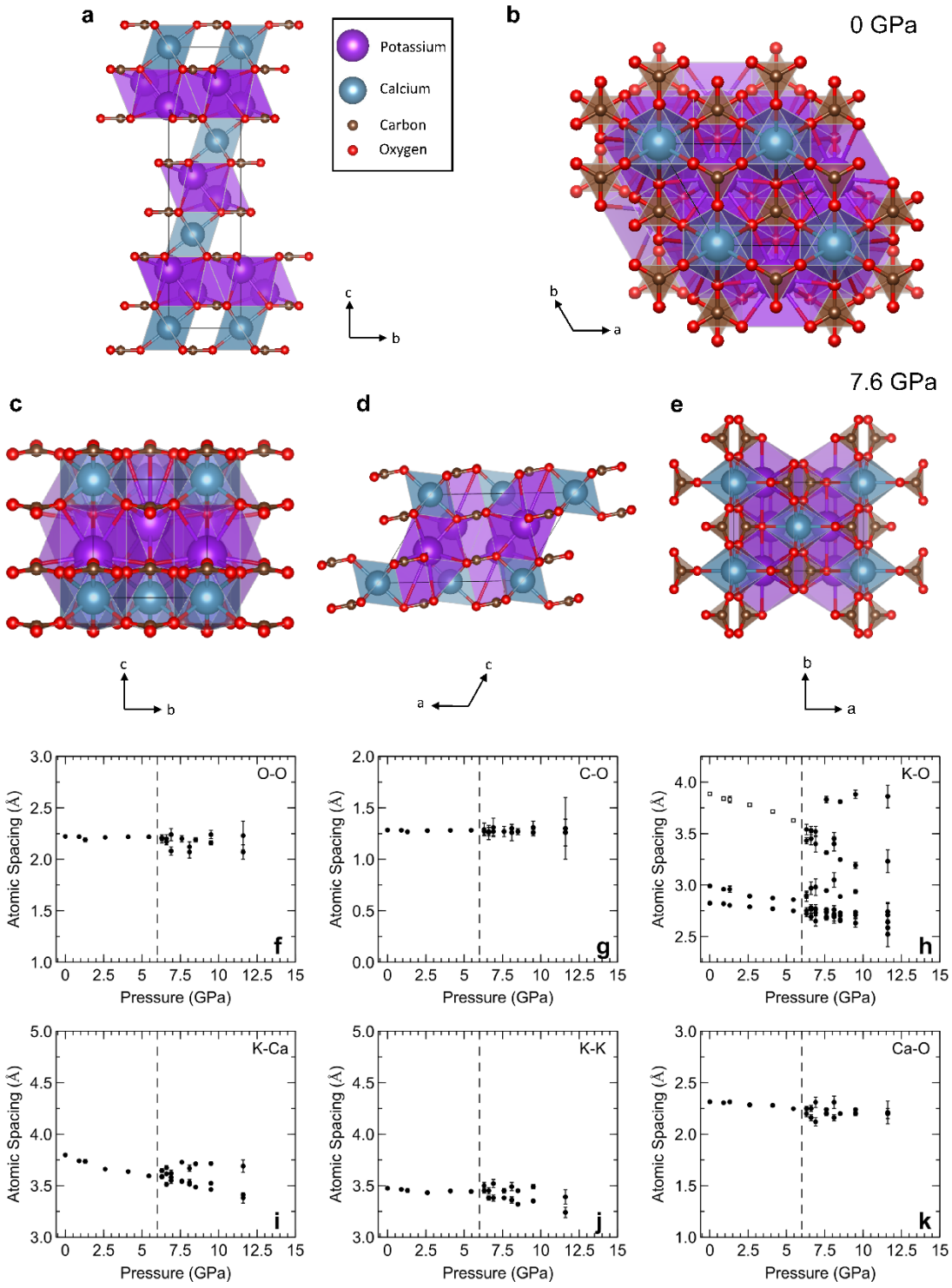

175

176 **Figure 1** Structural refinements of bütschliite and bütschliite-II at 0 and 7.6 GPa, respectively, from different perspectives (a-e).

177 Atomic spacings of bütschliite and bütschliite-II derived from single-crystal measurements (f-k). Note that the structures in (c-e)

178 are drawn with the K^+ ions in 12-fold coordination. The unfilled square symbols in (h) show distances between unbonded
179 potassium and oxygen atoms that become bonded after the phase transition.

180 The combined single crystal and powder pressure-volume data were recast into Eulerian
181 stress-strain coordinates and fit with a Birch-Murnaghan equation of state (Figure SI 1). The
182 equation of state was fit to the stress-strain data using an orthogonal distance regression to
183 account for uncertainties in both pressure and volume resulting in a bulk modulus of $K_0 =$
184 $46.9(17)$ GPa with an imposed value of $K_0' = 4$ (Figure 2f). The equation of state fit to the x-ray
185 diffraction data indicates that the structure is more compressible than the results from the first
186 principles calculations of Hou et al. (2022), but close to the results of Zhuravlev (2022). Our
187 values of K_0 is 23% smaller than the value calculated by Hou et al. (2022). Notably, our
188 measurements of the bütschliite low-pressure phase extend to higher pressures than the
189 calculations of Hou et al. (2022), as their calculations yield a $P\bar{1}$ phase intermediate between the
190 $R\bar{3}m$ and $C2/m$ phases at pressures between 3.3 and 10.3 GPa: this phase is not seen in the x-ray
191 diffraction data in this pressure range. In terms of elasticity, the discrepancy between the theory
192 and experiment appears to primarily involve the compressibility of the c-axis: the calculations of
193 Hou et al. (2022) underpredict the experimentally observed compressibility of this axis.

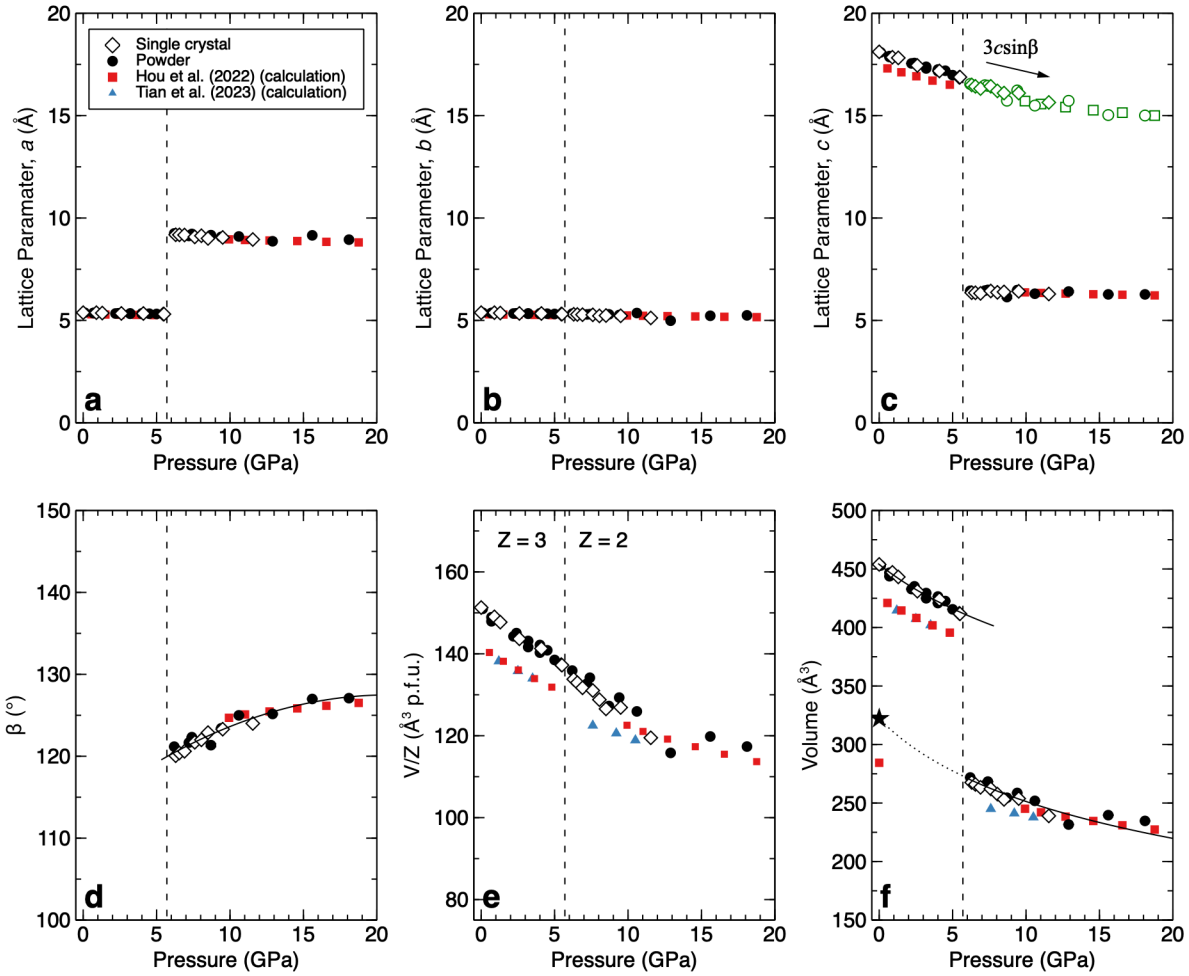

Figure 2 Lattice parameters (a-c), β-angles (d), formula unit normalized volumes (e), and unit cell volumes of bütschliite and bütschliite-II during compression (f). The green markers in (c) show the $3csin(\beta)$ trend, which is directly comparable to the c-axis in the low-pressure phase. The black star in (f) is the calculated zero-pressure volume of bütschliite-II from the method of Jeanloz (1981). Equation of state parameters for (f) are reported in the text. Fits only include the experimental x-ray data. The data point of Hou et al. (2022) at 10 GPa is in a metastable regime of the *C*2/*m* phase: they calculate that the $P\bar{1}$ structure is stable from 3.3 to 10.3 GPa. Tian et al. (2023) do not report lattice parameters or β-angles; the *C*2/*m* phase is stable in their calculations from either 3.3 or 3.5 GPa to 10.3 or 10.5 GPa (their paper is inconsistent in its reporting of the pressure of transitions). Error bars fall within the symbols.

3.2 Single Crystal and Powder X-ray Diffraction of Bütschliite-II

205 Bütschliite undergoes a phase transition between 5.5 and 6.0 GPa. Our lowest pressure
206 refinement of the bütschliite-II phase from the single crystal data is at 6.3 GPa. The high-
207 pressure phase crystallizes in the monoclinic system with *C*2/*m* symmetry (space group #12) and
208 Z = 2, with cell parameters at this pressure of *a* = 9.182(7) Å, *b* = 5.299(6) Å, *c* = 6.354(11) Å,
209 and $\beta = 120.06(3)°$. The volume change across the phase transition on a formula unit basis is
210 small but discontinuous, indicating that the transition is first-order (Figure 2e). This is in accord
211 with hysteresis observed in the transition using Raman spectroscopy, described below. Based on
212 the single-crystal data, there is a 2% density increase associated with the transition from the
213 hexagonal to monoclinic phase between 5.5 and 6.3 GPa. The small ΔV across the phase
214 transition indicates that the Clapeyron slope between the two phases is likely to be relatively flat,
215 which in turn suggests that the pressure of the phase transition is unlikely to have a robust
216 temperature dependence. The transition from the hexagonal to monoclinic phase is reversible,
217 with the high-pressure phase reverting to bütschliite on decompression below ~2 GPa. Following
218 the method of Jeanloz (1981), an equation of state was fit to the high-pressure bütschliite-II
219 phase (Figure SI 2) with parameters $V_0 = 322.2$ Å^3, $K_0 = 24.8(44)$ GPa, and $K_0' = 4.0(11)$
220 (Figure 2f). Our fit bulk modulus is 50% smaller than the value calculated by Hou et al. (2022).
221 And, the bulk modulus of bütschliite-II is substantially less than the bulk modulus of
222 $K_2Mg(CO_3)_2$-II, $K_0 = 58.4$ GPa, reported by Golubkova et al. (2015). The bulk moduli of the
223 bütschliite-I and -II phases are low relative to most other carbonates, but that of the low-pressure
224 phase is comparable to the bulk moduli of $BaCO_3$-witherite and Ag_2CO_3 (Wang et al. 2015;
225 Santamaria-Perez et al. 2023). Similarly, the lower bulk modulus of the high-pressure phase is
226 unusual, but not unprecedented for carbonates: a high-pressure phase in layered Ag_2CO_3 has a
227 bulk modulus of 26 GPa (Santamaria-Perez et al. 2023). A key aspect here is that the *C*2/*m*

symmetry phase appears to be stabilized at high pressures by its high compressibility. ~~: its inferred zero-pressure volume is larger than that of the low-pressure phase, but its low bulk modulus renders it volumetrically smaller at high pressures.~~

Notably, there is not particularly good agreement between the volumes and phase transition pressures of the theoretical calculations and experiments plotted in Figure 2. The first principles simulations of Hou et al. (2022) and Tian et al. (2023), carried out at 0 K, both predict phase transitions near 3.5 and 10.5 GPa, but the order of the transitions is different. Hou et al. (2022) reports a transition from the $R\bar{3}m$ phase to a triclinic $P\bar{1}$ structure at 3.3 GPa followed by a transition to the monoclinic *C*2/*m* structure at 10.3 GPa, while Tian et al. (2022) reports a transition to the monoclinic *C*2/*m* structure at 3.3–3.5 GPa and a transition to the triclinic $P\bar{1}$ structure at 10.3–10.5 GPa. The source of this disparity is unclear, as both simulations were conducted using the VASP software package, and the cut-off and convergence criteria of their calculations seem to be essentially identical. That said, the reported differences in enthalpies between the three phases at 0 K are quite small: near 10 GPa, less than 0.08 eV/formula unit reported by Hou et al. (2022), and less than 0.07 eV/atom according to Tian et al. (2023). The difference between the *C*2/*m* and the $P\bar{1}$ structures is even smaller, being less than 0.01 eV/formula unit (Hou et al. 2022) or 0.01 eV/atom (Tian et al. 2023) up to 12 GPa. As such, calculations at 0 K without thermal corrections might not accurately predict phase stabilities for such energetically close phases even at ambient temperatures. For comparison, Zhuravlev (2022) (using a different *ab initio* software package) predicts a shear instability to an unspecified structure at 5.8 GPa. There is also likely an effect of kinetics on the experimentally observed bütschliite-I to -II phase transition at 300 K: the transition is observed on the up-stroke near 6 GPa, and the reversion is observed on the down-stroke near 2 GPa. Accordingly, the equilibrium

transition may occur close to 4 GPa (from the mid-point between the up-stroke and down-stroke transition pressures) at 300 K. Consideration of kinetic effects thus might somewhat improve the agreement between theory and experiment with respect to the pressure of the first transition in this material.

In contrast to the low-pressure phase, where compression occurs predominantly along the *c*-axis of the hexagonal cell, rotation and interlayer shifting seem to be almost entirely responsible for the enhanced compressibility of the bütschliite-II phase. The trend of $3c\sin(\beta)$ in Figure 2c serves as an analogue for the interlayer spacing within the low-pressure phase, and shows that the interlayer compression is largely monotonic across the transition. The change in slope of the $3c\sin(\beta)$ trend is likely a result of changing K-O bond lengths (discussed below). All axial parameters follow relatively flat linear trends on compression while the β-angles follow an increasing quadratic trend, with $\beta(P) = -0.033P^2 + 1.371P + 113.204$ (Figure 2d). This increase in β-angle directly reflects the pressure-induced lateral shifting between layers (e.g., Fig. 1d). It is this interlayer shifting that likely renders the high-pressure phase elastically softer than the low-pressure bütschliite phase: the complementary effects of carbonate group rotation and layer shifting provide additional means of compaction that are unavailable to the low-pressure phase. Beyond the rotation and layer shifting, the overarching structural similarities of the two phases produce pressure-induced trends of bond valence sums (Kunz and Brown 1995) that appear continuous between the two phases under compression: both cations and the oxygen ions have bond valence sums that monotonically increase over the pressure range of our single-crystal measurements.

The phase transition to bütschliite-II results in the bifurcation of several atomic distances and bond lengths (Figure 1f, g, j, k). The high-pressure phase gives rise to two unique C-O and

Ca-O bond lengths. The evolution of the K-O bond lengths is more complex. Within both the bütschliite and *C*2/*m* phases, potassium has been generally viewed as being in nine-fold coordination: in the *C*2/*m* phase, the 9-coordinate geometry is that of a distorted tri-capped trigonal prism (e.g., Akella and Keszler 1995a,b). However, within the $K_2Ca(CO_3)_2$ *C*2/*m* phase, depending on the radius of the coordination sphere of potassium, the K^+ cations may be viewed as undergoing a coordination change, initially forming elongated [KO_{12}] cuboctahedra (perhaps more appropriately viewed as 9+3 coordination), with the longer K-O bond lengths being coupled to the rotation of the [CO_3] anions (Figure 1h). Here, we view K-O distances of 3.3 Å and less as being clearly within the coordination sphere of the K ion, based on the maximum eight-fold K-O distances in a survey of K-bearing compounds being 3.17 Å (Wood and Palenik 1999), and the typical difference in bond distance between eight and twelve-fold coordination being 0.13 Å (Shannon 1976). Such distances are accessed by additional oxygens above ~8 GPa (Figure 1h); the general trajectory of the more distant K-O distances (Fig. 1h) indicates that this transition to higher coordination is progressive following the transition to the high pressure phase (with those distances closer than ~3.5-3.6 Å potentially being viewed as part of a secondary coordination distance, giving rise to 9+2 or 9+3 cooordination).

With increasing compression, the [CO_3] units become more oblique with respect to the a-axis and, as shown in Figure 3, there is a direct line-of-sight interaction between the K^+ ion and the neighboring carbon ion that is coordinated to the three additional oxygens that approach the coordination sphere of the potassium. Repulsion between the C and K atoms likely contribute to the rotation of the [CO_3] units, as the C-K distance remains constant around 3.25 Å during compression: increasing pressure does, however, induce a rotation of the carbonate units. This shift in geometry rotates two oxygens closer to the potassium ion, and one further away: as such,

297 at 9.5 GPa, the local coordination of potassium might be viewed as 11-fold, or 9+2 coordinated.
298 Notably, if the C-K distance is indeed near some minimum critical value, then the rotation of
299 [CO_3] units and change in β-angle can be interpreted as structural distortions which serve to
300 maintain this value.

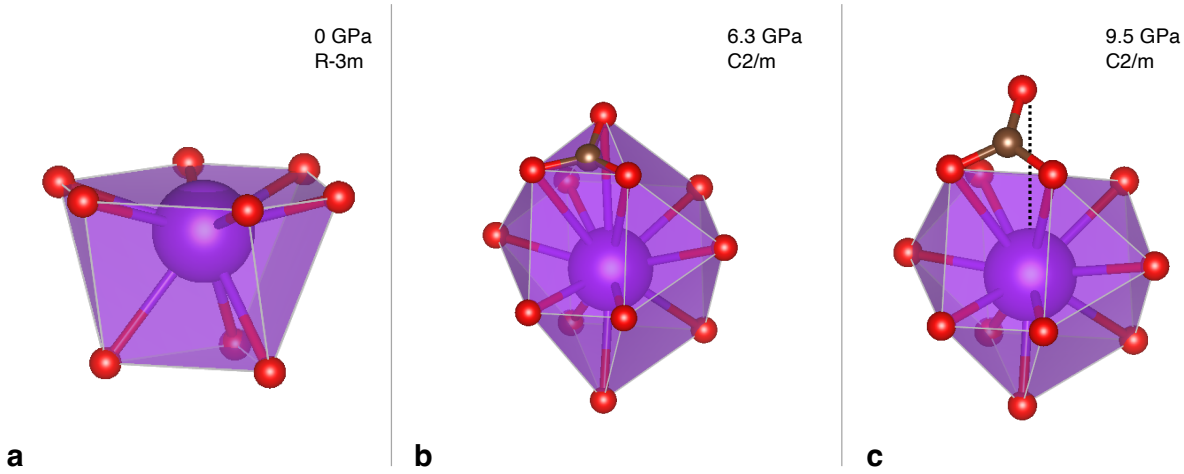

301
302
303 **Figure 3** K-O coordination environments of the $R\bar{3}m$ (a) and $C2/m$ (b,c) phases of bütschliite. Coordination progresses from 9-
304 fold in (a), to 12-fold (9+3) in (b), to 11-fold (9+2) in (c). The dotted line in (c) shows the oxygen atom leaving the potassium
305 coordination sphere.

306 We quantify the degree of tilting of the [CO_3] units by measuring the angle θ, formed by the
307 intersection of the (001) plane with a plane passing through the three oxygens atoms of the [CO_3]
308 unit, as a function of pressure. This trend is well characterized by a quadratic polynomial in
309 pressure, with $\theta(P) = -66.86 + 15.95P - 0.79P^2$ (**Figure *4***).

310 Our powder diffraction data on bütschliite access considerably higher pressure
311 conditions, up to 67.5 GPa (Figure SI 3). These data show strong evidence for multiple higher
312 pressure phase transitions, for which the pressures of occurrence are more accurately determined

313 by Raman spectroscopy. Nevertheless, clear evidence is seen for three transitions between ~26
314 and 40 GPa, although indexing of these phases proved challenging due to poor crystallinity/weak
315 diffraction patterns, as well as probable preferred grain orientation in the high-pressure phases.
316 New diffraction peaks associated with these phases are shown by arrows in Figure SI 3b. A key
317 aspect here is that there is continuity of several features in the diffraction patterns throughout the
318 pressure range to 67.5 GPa (Figure SI 3). This observation provides a general indication that the
319 overall layered topology of the structure persists, with moderate symmetry changes, to the
320 highest pressures of these measurements at 300 K.

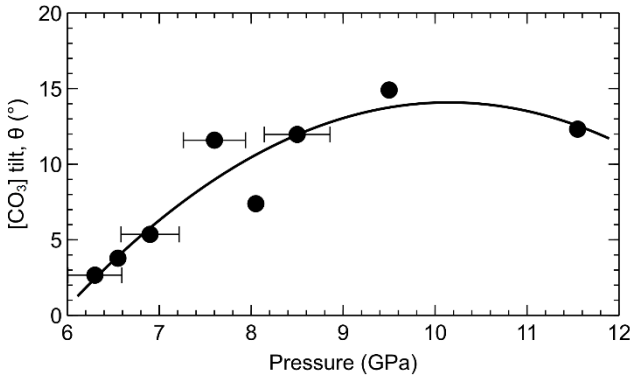

321

322 **Figure 4** Tilt of [CO_3] units in the bütschliite-II phase as a function of pressure, derived from single-crystal XRD refinements.
323 The angle θ is formed by the intersection of the (001) plane with a plane passing through the three oxygen atoms in a [CO_3] unit.
324 The fit is a quadratic fit intended to guide the eye.

325

326 **3.3 Raman Spectroscopy Overview**

327 Our ambient spectrum of the synthesized bütschliite (Figure 5) is in good agreement with
328 previous measurements (Arefiev et al., 2019) and calculations (Caracas and Bobocioiu, 2011).

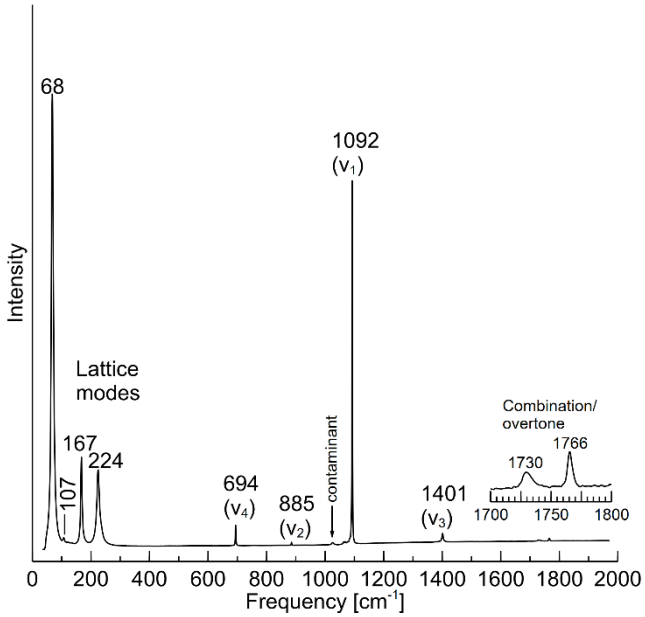

Figure 5 Raman spectrum of synthetic bütschliite-I taken under ambient conditions.

Representative spectra taken on compression up to 94 GPa, along with mode shifts, are plotted in Figure 6. Our Raman measurements access substantially higher pressures than the XRD measurements, and we documented multiple phase transitions at elevated pressures in detail in the Raman spectral experiments which are discussed in the following sections.

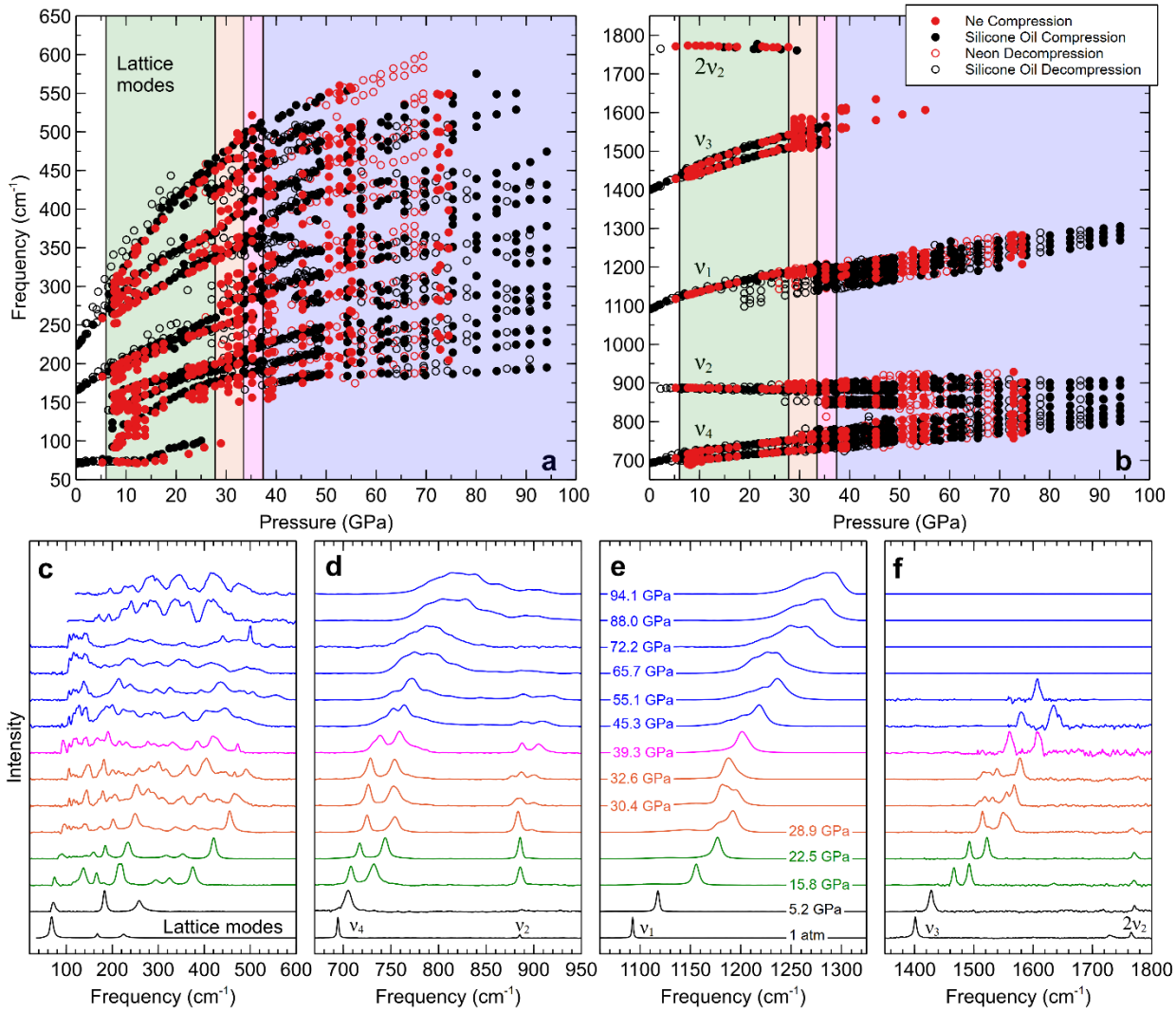

Figure 6 Mode shifts (a-b) and representative spectra (c-f) of bütschliite on compression to 94 GPa. The first appearances of new phases are marked by lines at 6.0, 27.8, 33.5, and 37.4 GPa and the colors correspond to different phase regimes: bütschliite-I is black, bütschliite-II is green, bütschliite-III is orange, bütschliite-IV is magenta, and bütschliite-V is blue. For clarity, the largest peak intensities have been normalized to the same amplitude across panels c-f.

3.4 Raman Spectra of Bütschliite-I

Factor group analysis of bütschliite-I yields

$$\Gamma_{optic} = 4\mathrm{A_{1g}} + \mathrm{A_{1u}} + \mathrm{A_{2g}} + 4\mathrm{A_{2u}} + 5\mathrm{E_u} + 5\mathrm{E_g}. \quad (1)$$

In this irreducible representation, the A_{1g} and E_g modes are Raman-active. We observe 10 peaks in the ambient bütschliite spectrum (Figure 5), with eight first order ($5E_g$, $3A_{1g}$) and two second order modes (assignments are derived from Caracas and Bobocioiu, 2011): six of these peaks are resolvable once the sample is loaded into the DAC with a pressure medium.

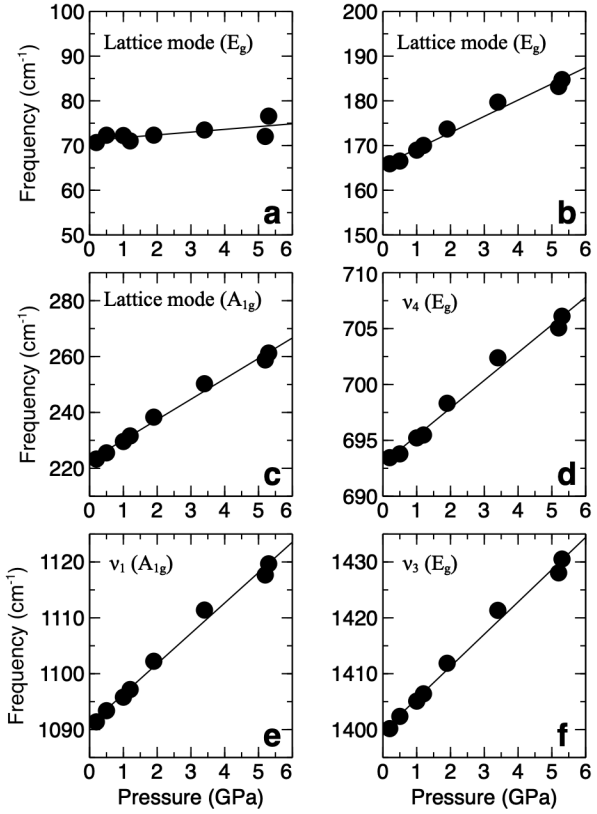

Figure 7 Mode shifts of bütschliite-I under compression up to the transition to the *C*2/*m* phase.

All observed modes exhibit positive linear frequency shifts with pressure up to the first phase transition to the *C*2/*m* structured phase (Figure 7 and Table 1). The symmetric (ν_1) and asymmetric (ν_3) stretches have similar pressure shift rates: 5.44 and 5.78 cm^{-1}/GPa, respectively. The in-plane bend shifts at a considerably slower rate, with a value of 2.48 cm^{-1}/GPa.

Assignment	Symmetry	Measured initial frequency, v_0 (cm^{-1})	dv_i/dP (cm^{-1}/GPa)	γ_i
Lattice mode	E_g	68	0.62(26)	0.43
Lattice mode	E_g	107	--	--
Lattice mode	E_g	167	3.64(19)	1.03
Lattice mode	A_{1g}	224	7.31(28)	1.54
In-plane bend, v_4	E_g	694	2.48(11)	0.17
Out-of-plane bend, v_2	A_{1g}	885	--	--
Symmetric stretch, v_1	A_{1g}	1092	5.44(20)	0.24
Asymmetric stretch, v_3	E_g	1401	5.78(23)	0.19
Overtone, $2v_2$ (IR)		1730	--	--
Overtone, $2v_2$ (Raman)		1766	--	--

Table 1 Symmetry assignments, measured initial frequencies, frequency-pressure derivatives, and mode-Grüneisen parameters of bütschliite-I.

The lattice modes exhibit larger variations in their pressure shifts and are, based on their mode-Grüneisen parameters, more anharmonic. The A_{1g} lattice mode with an initial frequency of 224 cm^{-1} shows the largest deviation from harmonicity among all observed modes: the large pressure-shift of this mode, which is associated predominantly with translations of the carbonate group along the c-axis of the structure (Caracas and Bobocioiu, 2011), likely directly reflects the large compressibility of the *c*-axis observed within the diffraction experiments. Although the lack of thermal expansion data on bütschliite precludes calculation of a bulk thermodynamic Grüneisen parameter for this phase, it is clear from Table 1 that the largest contributors to this parameter are, as expected, among the lattice vibrations.

3.5 Raman Spectra of Bütschliite-II

The first signs of a phase transition observed in the Raman data occur at 6.5 GPa, and the spectrum at this pressure likely corresponds to a mixed-phase regime. At this pressure, the first hint of three new lattice modes appears between 110 to 150 cm^{-1}. The highest frequency lattice mode broadens asymmetrically prior to splitting into three peaks, and ν_4 and ν_3 broaden asymmetrically prior to splitting into two peaks each. By 7.2 GPa the sample appears to be fully converted to the bütschliite-II phase. While the ν_2 vibration is weakly present in the ambient bütschliite spectrum, it becomes, for the most part, unresolvable once the sample is loaded into the DAC with a pressure medium. The change in symmetry to *C*2/*m* in the high-pressure phase results in a substantial increase in the amplitude of the ν_2 peak during compression (Figure 8b).

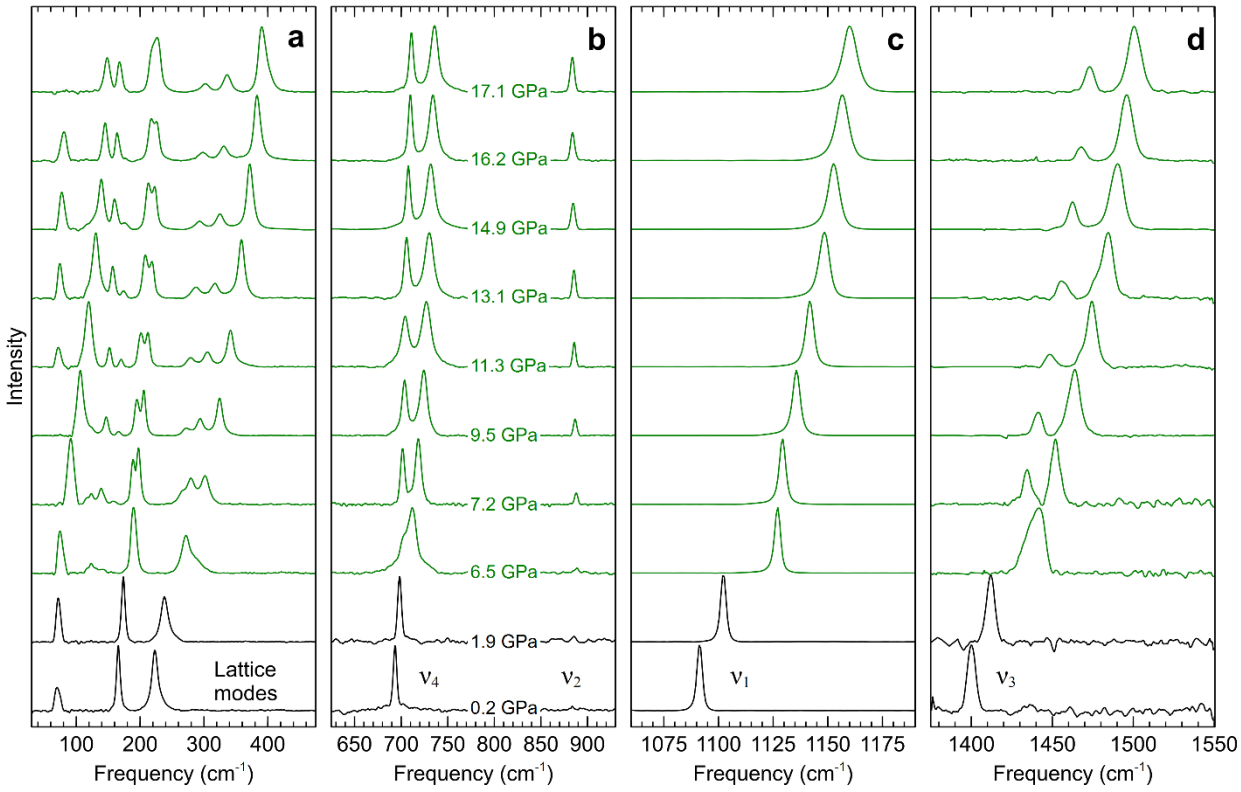

Figure 8 Raman spectra showing the transition from bütschliite-I (black) to bütschliite-II (green). For clarity, the largest peak intensities have been normalized to the same amplitude across the panels.

Factor group analysis of the bütschliite-II structure yields

383 $$\Gamma_{optic} = 9\mathrm{A_g} + 6\mathrm{A_u} + 6\mathrm{B_g} + 9\mathrm{B_u}. \quad (2)$$

384 Here, the A_g and B_g modes are Raman active. Symmetry assignments and pressure shifts
385 of the bütschliite-II carbonate modes are reported in Table 2 and Figure 9. The mode Grüneisen
386 parameters are calculated at high pressure using a Taylor expansion of $K(P)$ with a truncating
387 value of K_0'' (i.e., $K_0'' = \frac{1}{9K_0}[63K_0' - 9K_0'^2 - 143]$: Birch, 1978). The frequency shifts with
388 pressure of all modes are positive, except for the ν_2 and $2\nu_2$ vibrations (the CO_3 out-of-plane
389 bend and its overtone). The negative frequency shift of the ν_2 mode during compression has
390 previously been explained for the aragonite structure (*Pmcn* symmetry) as resulting from the
391 dominance of a negative force constant, produced by coupling between neighboring carbonate
392 anions, over the positive force constant associated with the bending vibration of an isolated
393 carbonate ion during compression (Decius, 1955; Kraft et al., 1991).
394

Assignment	Symmetry	Fit initial frequency, v_0 (cm^{-1})	High pressure frequency, v_P (cm^{-1})	dv_i/dP (cm^{-1}/GPa)	γ_i
In-plane bend, v_{4a}	B_g	690.73(54)	702	1.18(3)	0.11
In-plane bend, v_{4b}	A_g	708.31(59)	718	1.56(3)	0.14
Out-of-plane bend, v_2	A_g	889.69(62)	888	-0.30(3)	-0.02
Symmetric stretch, v_1	A_g	1097.83(178)	1129	4.26 – 0.07P	0.22
Asymmetric stretch, v_{3a}	B_g	1405.60(73)	1435	3.79(4)	0.17
Asymmetric stretch, v_{3b}	A_g	1401.04(267)	1452	7.03 – 0.14P	0.27
Overtone, $2v_2$†	?	1776.46(218)	1773	-0.37(11)	-0.01

395 **Table 2** Symmetry assignments, fit zero pressure frequencies, measured initial high-pressure frequencies, frequency-pressure
396 derivatives, and mode-Grüneisen parameters (γ_i) of bütschliite-II evaluated at 7.3 GPa. †Evaluated at 7.6 GPa (no peak observed
397 at 7.3 GPa).

398
399

Negative frequency shifts of the ν_2 or $2\nu_2$ mode during compression have also been observed in a range of carbonate minerals, including calcite, strontianite, magnesite, dolomite, shortite, and bästnasite (Gillet et al., 1993; Vennari and Williams, 2018; Bayarjargal et al. 2018; Vennari et al., 2018; Efthimiopoulos et al., 2019; Vennari and Williams, 2019). The trajectory of the ν_2 mode toward lower frequencies upon compression has substantial consequences for the evolution of the bütschliite spectrum, contributing to the development of a complex resonance phenomenon between the ν_2 and ν_4 vibrations observed at higher pressures.

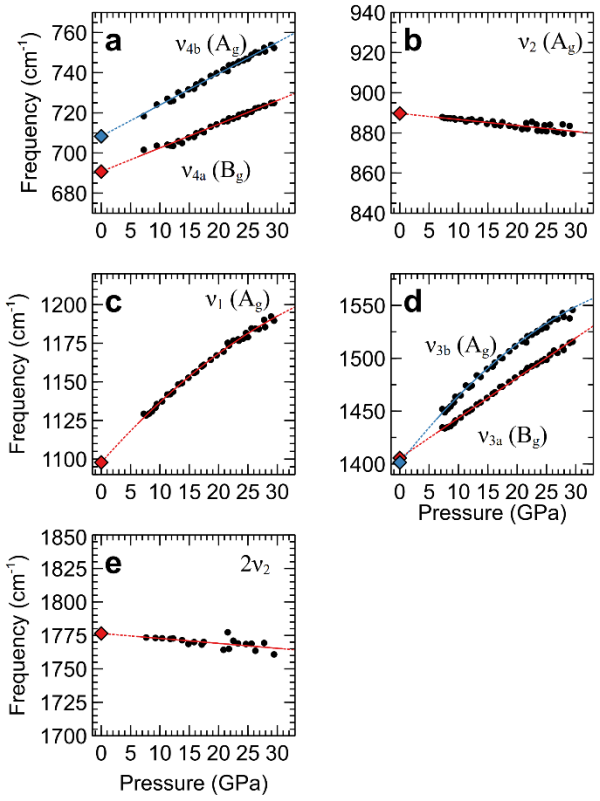

Figure 9 Carbonate mode shifts of bütschliite-II. Blue and red diamonds show extrapolations to zero pressure.

The spectrum of bütschliite-II is remarkably similar to the ambient-pressure spectrum of $Sr_2Mg(BO_3)_2$ presented by Lv et al. (2018), which also belongs to the *C*2/*m* space group, providing independent confirmation of our single-crystal refinements. In order to semi-

quantitatively compare the spectra of the borate relative to the carbonate in $Sr_2Mg(BO_3)_2$ and $K_2Ca(CO_3)_2$, we use the quantity

$$\xi_{A-B} = \sqrt{\frac{Z_A Z_B}{r^3 \mu}} \tag{3}$$

where *A* and *B* are bonded elements, *Z* is the charge, *r* is the bond length (with values taken from Shannon, 1976), and $\mu = m_A m_b/(m_A + m_B)$ is the reduced mass. This relation is simply derived from Coulombic interactions coupled with harmonic oscillators. For the anions under consideration, $\xi_{B-O} = 0.61$ and $\xi_{C-O} = 0.75$. The ratio of these quantities,

$$\chi = \frac{\xi_{C-O}}{\xi_{B-O}} \tag{4}$$

serves as a scaling factor with $\chi = 1.23$. Application of this scaling factor to the ambient pressure fits of the bütschliite-II carbonate modes recovers the borate mode frequencies of $Sr_2Mg(BO_3)_2$ to within 0.2 to 7.5%, with the largest deviation being for the asymmetric stretching vibration of the carbonate group (ν_3), which is anticipated to be substantially affected by the surrounding cations.

The spectra of bütschliite-II also show some novel spectroscopic features (Figure 10). Specifically, Fermi resonance occurs when the wave functions of two vibrational modes with the same symmetry and similar energies mix. In vibrational spectra, the phenomenon manifests as the frequencies of two resonating peaks, ν_- and ν_+, following a hyperbolic trajectory and exchanging intensity. We observed a Fermi resonance in the lattice modes of bütschliite-II, spanning from 9 to 29 GPa (Figure 10). By comparing the spectra of the bütschliite-II with the calculated spectrum of $Sr_2Mg(BO_3)_2$ from Lv et al. (2018), we are able to infer that the resonating modes each have A_g symmetry and involve vibrations of K^+ against $[CO_3]$ units. The coupling constant, representing the semi major axis of the hyperbola in pressure-frequency

space, is δ = 9.27 cm^{-1} and the maximum resonance occurs at 19.7 GPa. Following Shimizu (1985), we calculated the unperturbed frequencies ν_a and ν_b (Figure 10b), which represent the frequency trajectories the peaks would follow in the absence of resonance:

$$\nu_a = \frac{\nu_+ + \nu_- + \sqrt{(\nu_+ - \nu_-)^2 - 4\delta^2}}{2} \quad (5)$$

$$\nu_b = \nu_+ + \nu_- - \nu_a \quad (6)$$

A notable feature of the bütschliite-II Fermi resonance is the nearly linear trajectory of the high frequency resonating peak, ν_+ (Figure 10b). Despite the asymmetric trajectories of the resonating peaks, the diagnostic intensity exchange between the peaks is clearly present over the duration of the resonance (Figure 10c). The resonating modes, and indeed all Raman-active lattice modes in the *C*2/*m* phase, only involve motion of the carbonate and potassium ions. The ν_+ vibration involves intralayer motion, while the ν_- vibration involves interlayer stretching and is dominated by the K-CO_3 motion mostly along the *c*-axis. This axial direction is more compressible than the direction associated with the vibration in the *ab*-plane of ν_+, resulting in the pronounced stiffening of the ν_- mode during compression. Hence, this resonance provides separate confirmation of the relative compressibilities of the different axes of the crystal that were characterized using single-crystal diffraction, and verifies that these structural trends persist to substantially higher pressures than the single-crystal data probe.

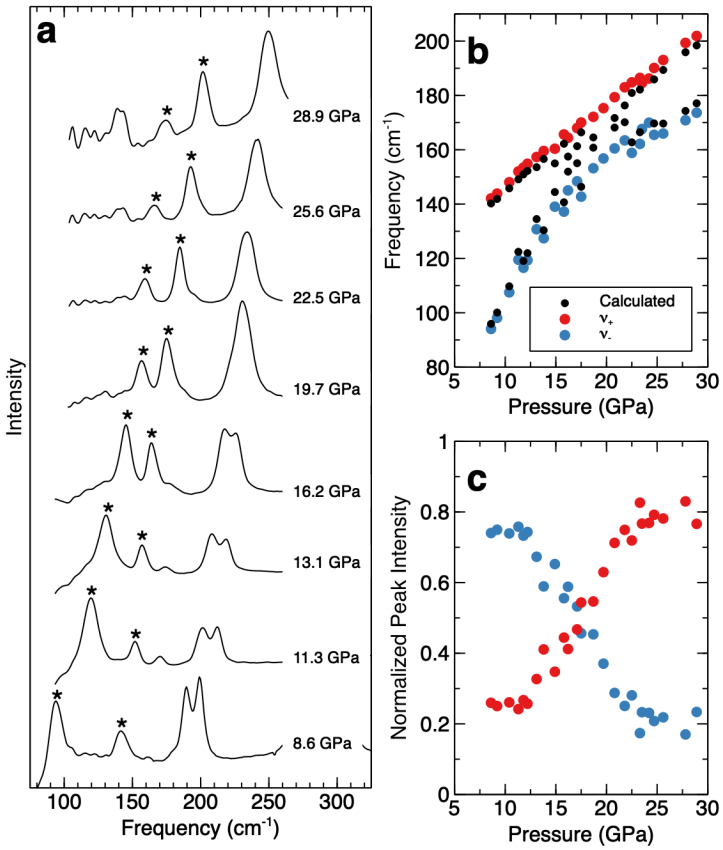

451

452 **Figure 10** Fermi Resonance in bütschliite-II. Raman spectra of the lattice modes during compression (a). Resonating peaks are
453 marked with asterisks. Measured frequencies of resonating peaks and calculated unperturbed frequencies (b). Normalized
454 intensities of the resonating peaks (c).

455

456 **3.6 Subsequent phase transitions**

457 We observe three more phase transitions in the Raman spectra, which are also manifested in the
458 powder diffraction data (Figure SI 3): because of their narrow spacing in pressure, the Raman
459 data provide better constraints on the transition pressures. There are two transitions to phases
460 with limited stability ranges, bütschliite-III and bütschliite-IV, followed by a transition to
461 bütschliite-V, which appears to be stable up to our highest-pressure measurement at 94.1 GPa.
462 The first indications of a transition from bütschliite-II to bütschliite-III occur at 27.8 GPa, with

463 the appearance of a low-frequency peak associated with the ν_1 vibration at 1179 cm^{-1} (Figure
464 11c). In the next pressure step, at 28.9 GPa (shown in Figure 11c), the lattice modes broaden and
465 decrease in intensity, a new high-frequency component associated with the ν_2 vibration grows in
466 at 898 cm^{-1}, the low-frequency component of the ν_1 vibration increases in intensity, and high-
467 frequency components of both ν_3 peaks appear. The bütschliite-II ν_1 peak loses intensity with
468 increasing pressure and is fully absent by 35.2 GPa. Hence, the increase in band multiplicity of
469 the ν_2 and ν_3 peaks are compatible with an expanded unit cell and/or a larger number of distinct
470 carbonate groups within bütschliite-III relative to the *C*2/*m* structured bütschliite-II. This inferred
471 decrease in symmetry is supported by the x-ray data, which show a bifurcation of the d-spacing
472 associated with the $(20\bar{2})$ plane at ~26 GPa (Figure SI 3a). The lower frequency of the symmetric
473 stretch (ν_1) in bütschliite-III might be associated with a lower force constant/longer distance of
474 the C-O bonds, while the higher frequency components of the asymmetric stretches (ν_3) might
475 indicate a stronger interaction with neighboring cations (possibly within a subset of carbonate
476 sites). The net decrease in symmetric stretching (ν_1) frequency at this transition is roughly 15
477 cm^{-1}; this is a substantially smaller decrement than that associated with the onset of 3+1
478 coordination of carbonate groups (Vennari and Williams 2018; Vennari et al., 2018), which
479 generates a decrement of ~50 cm^{-1}. This could be the triclinic $P\bar{1}$ structure predicted by Hou et
480 al. (2022) to occur at 3.3 GPa, and Tian et al. (2023) to become stable at 10.3 or 10.5 GPa. While
481 we do not preclude this possibility, it is notable that Hou et al. (2022) predicts essentially
482 constant C-O distances between the *C*2/*m* and $P\bar{1}$ phases, which does not seem fully consistent
483 with the change in the frequency of the symmetric stretch (ν_1) that we observe. In passing, we
484 note that the clear doublet associated with the ν_4 vibrations likely precludes this phase from

485 being associated with the nyererite ($Na_2Ca(CO_3)_2$) structure: only a single ν_4 band is observed in
486 this structure (Vennari et al. 2018; Rashchenko et al. 2018).

487 The transition to bütschliite-IV occurs around 30.4 GPa in Ne. The onset of this phase is
488 marked by the concomitant splitting of the ν_2 vibration into a triplet and of the ν_3 vibration into a
489 multiplet of peaks, as well as a bifurcation of the $(11\bar{1})$ spacing in the x-ray data at ~32 GPa
490 (Figure SI 3a). There is also an increase in the intensity of the lattice mode around 400 cm^{-1}. By
491 35.2 GPa only a hint of the lowest frequency peak of the ν_2 triplet remains. At 38.4 GPa ν_3
492 reverts back to two peaks and the low frequency peak associated with ν_4 starts to broaden. By
493 39.3 GPa, the components of the ν_4 doublet have become substantially asymmetric. In this
494 instance, the transition is relatively subtle: no major shifts in vibrational bands occurs, but there
495 are changes in band multiplicities, with new bands being observed.

496 The transition to bütschliite-V is more dramatic, and occurs between 37.4 and 39.7 GPa
497 in silicone oil and above 39.3 GPa in Ne. At 45.3 GPa, ν_1 has split into several peaks (with at
498 least two new components emerging on its low frequency side), and the ν_4 and ν_2 peaks become
499 significantly broadened and distorted. Splitting of the ν_1 vibration indicates the presence of
500 multiple (possibly 4) distinct carbonate units within the unit cell, and the lowered frequency of
501 these bands implies that a portion of the C-O bonds in the structure have weakened. The ν_3
502 vibration becomes unresolvable beyond 50.6 GPa. The convergent trajectories of the ν_2 and ν_4
503 vibrations result in a complex resonance phenomenon that initiates at around 70 GPa (Figure 6b).

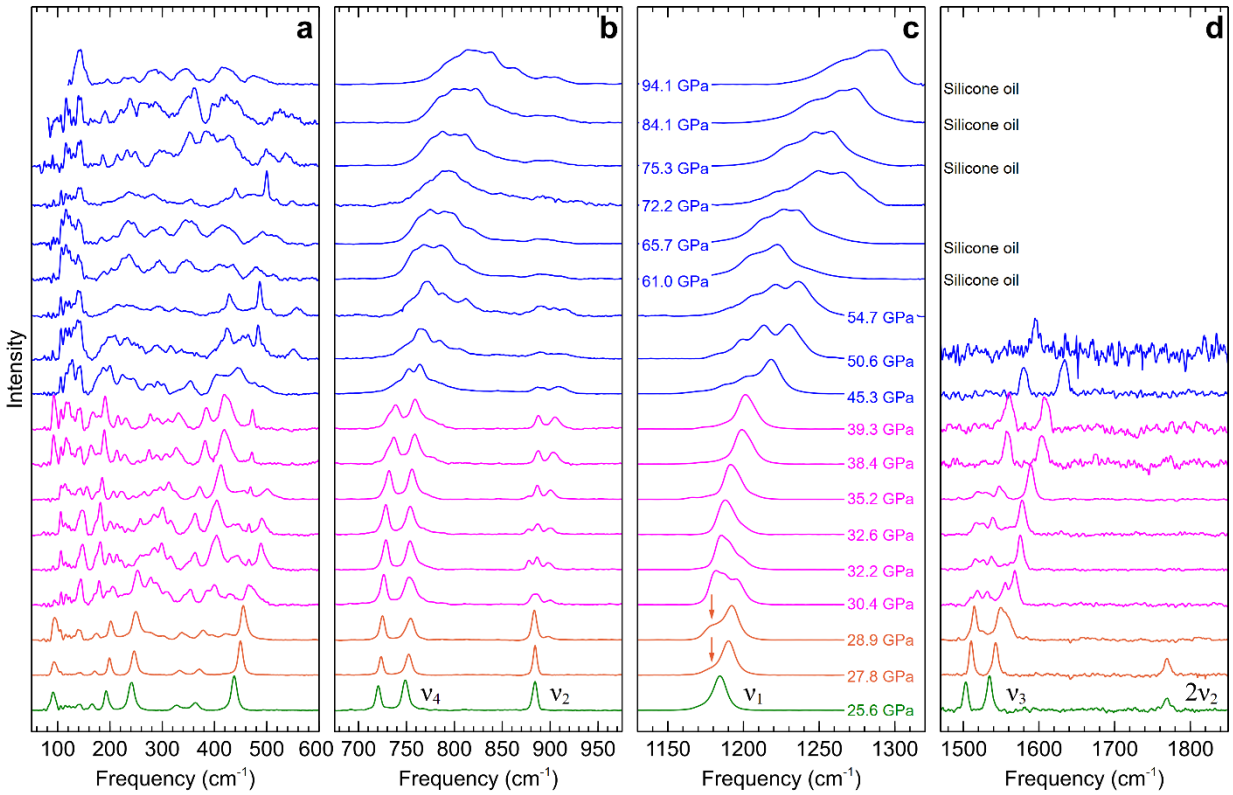

Figure 11 Raman spectra showing phase transitions from bütschliite-II through bütschliite-V. For clarity, the largest peak intensities have been normalized to the same amplitude across the panels. Unlabeled spectra were measured with the sample in a Ne PTM. Bütschliite-II is shown in green, bütschliite-III in orange, bütschliite-IV in magenta, and bütschliite-V in blue.

The separation between the ν_2 and ν_4 vibrations vanishes near 70 GPa, and the coalesced peaks move together as a single unit upon further compression. While there is no evidence to suggest that the wave functions of the two vibrations are mixing, the energy of the vibrations are clearly becoming similar. In effect, the in-plane and out-of-plane bending vibrations of the carbonate unit have become energetically identical, and components associated with the two types of molecular vibrations span across a frequency range approaching 150 cm^{-1}. Given the breadth of this bending region, it is certainly possible that combination bands of lattice modes as well as possible difference modes may be resonance enhanced by the bending vibrations, contributing minor, and possibly broad, peaks to this spectral region. A similar phenomenon was

observed in dolomite-III (Vennari and Williams, 2018) at similar pressures, and could possibly be an intrinsic feature of low-symmetry double carbonates subjected to very large compressions.

Notably, there is no indication of an increase in coordination associated with the carbonate group towards a 3+1 coordination, as has been observed in dolomite-III and shortite under pressure (Vennari and Williams 2018; Vennari et al. 2018). The principal manifestation of this change, a softening or lowered frequency of the ν_1 symmetric stretching vibration, does not occur up to 94 GPa in this material. This maintenance of the three-fold coordinate carbonate unit can likely be correlated with the maintenance of the layered-like overarching structure associated with the two lowest pressure phases: the next-closest oxygen to the carbonate units typically defines the edge of a cation polyhedron (e.g., Figure 1).

3.7 Compressibility of compositionally and structurally diverse carbonate phases

The evident rigidity of trigonal [CO_3] units in solid carbonate phases indicates that the cations play a dominant role in volumetric reduction during isothermal compression. Here, we explore the relationship between cation radius and compressibility for three groups of compositionally diverse and geologically important carbonate mineral structures: the broadly-defined "double carbonates" including bütschliite, the calcite-structured group, and the aragonite-structured group.

Figure 12 shows the relationship between the isothermal bulk modulus, K_T, and average non-carbon cation radius (a proxy for bond strength) for minerals belonging to each of the three carbonate groups listed above. In the case of the double carbonates, the cation radius is determined by weighting each cation radius by its stoichiometric subscript and dividing by the total number of cations (excluding carbon) in the chemical formula. It can clearly be seen that

the value of the bulk modulus decreases with increasing cation radius. A linear fit to the double carbonate data yields $K_T = -94.7(21)r + 175.0(20)$ and a linear fit to all data points yields $K_T = -82.4(11)r + 161.3(12)$. While the separate structures and stoichiometries present in Figure 12 may each have modestly different trends (with the trend of the transition metal-bearing calcites having been noted previously by Sawchuk et al. 2021), the overarching trends are roughly comparable. Figure 12 thus illustrates a rather simple effect: the compaction of the carbonates is largely modulated by their charge-balancing cations. Deviations from this general trend (such as might be the case for bütschliite-II) may reflect the presence of more complex compressional mechanisms beyond simple compaction of the cation sites (such as angle changes, carbonate group rotations, and/or coordination changes).

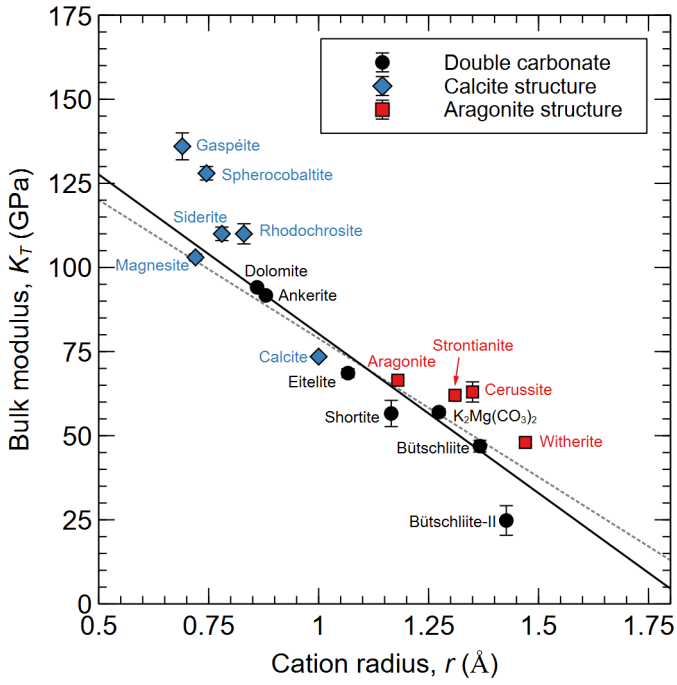

Figure 12 Isothermal bulk moduli as a function of cation radius for a suite of structurally and compositionally diverse carbonate minerals. The solid black line is a fit to the double carbonates only and the dotted gray line is a fit to all data. Cation radii are taken from Shannon (1976). Bulk moduli data are from: bütschliite and bütschliite-II ($K_2Ca(CO_3)_2$, this study); spherocobaltite ($CoCO_3$, Chariton et al., 2017); eitelite ($Na_2Mg(CO_3)_2$) and $K_2Mg(CO_3)_2$ (Golubkova et al., 2015); siderite ($FeCO_3$, Lavina et al., 2010); rhodochrosite ($MnCO_3$, Merlini et al., 2015); aragonite ($CaCO_3$, Palaich et al., 2016); calcite ($CaCO_3$, Redfern and Angel, 1999); dolomite and ankerite ($CaMg(CO_3)_2$ and $Ca(Fe,Mg,Mn)(CO_3)_2$, Ross and Reeder, 1992); gaspéite ($(Ni,Mg)CO_3$, Sawchuk et al., 2021); shortite ($Na_2Ca_2(CO_3)_3$, Vennari et al., 2018); strontianite and witherite ($SrCO_3$ and $BaCO_3$, Wang et al., 2015); cerussite ($PbCO_3$, Yu-Feng et al., 2013); and magnesite ($MgCO_3$, Zhang et al., 1997).

4. Conclusions

Bütschliite is a highly compressible mineral that undergoes a series of four high-pressure phase transitions during isothermal compression up to 95 GPa. Compression of the ambient-pressure phase is highly anisotropic, with contraction along the *c*-axis (i.e., reductions in K-O and K-Ca distances) accounting for most of the volume change in this material. Our results suggest that the ambient-pressure bütschliite phase is likely stable to a depth of about 180 km within the Earth; this stability range in depth is likely to be largely independent of geothermal variations.

Bütschliite converts to a monoclinic phase with *C*2/*m* symmetry at ~6 GPa. Compression of this phase is controlled by interlayer shifting and rotation of the carbonate groups. This new compression mechanism provides additional means of compaction that are unavailable to the low-pressure phase, and results in a more compressible structure. The enhanced compressibility of the *C*2/*m* structure likely augments the stability of the bütschliite-II phase, as the large $P\Delta V$ difference between the $R\bar{3}m$ phase (in its metastable region above ~6 GPa) and the more compressible *C*2/*m* phase (and possibly the hypothesized $P\bar{1}$ phase) will result in an expanded stability field in the phase diagram. A Fermi resonance observed in the lattice modes of bütschliite-II provides independent confirmation of the relative compressibilities of different axes that were characterized with single-crystal x-ray diffraction. Our results, when kinetic effects are considered, indicate that bütschliite inclusions found in deep-formed diamonds (e.g., Logvinova et al., 2019) likely initially crystallized as the *C*2/*m* phase and reverted to the $R\bar{3}m$ phase during ascent through the mantle or following emplacement. Furthermore, our results also indicate that previous phase equilibrium experiments in alkali carbonate systems (e.g., Shatskiy et al., 2015) may not have crystallized bütschliite at 6 GPa, but rather the *C*2/*m* phase, which reverts to bütschliite upon quenching.

Subsequent phase transitions observed in the Raman data show progressive distortion of carbonate units, ultimately giving rise to new distinct carbonate units within the structure and possibly expansion of the unit cell. Nevertheless, the overarching layer-type structure appears to be maintained at 300 K across these transitions. The stability of bütschliite-V to very high pressures suggests that this phase could, if stable at high temperatures, play an important role in deep Earth alkaline carbonate storage and magmatism.

Statements and Declarations

All authors certify that they have no affiliations with or involvement in any organization or entity with any financial interest or non-financial interest in the subject matter or materials discussed in this manuscript.

References

Abersteiner A, Golovin A, Chayka I, Kaminetsky V, Goemann K, Rodemann T, Ehrig K (2022) Carbon compounds in the West Kimberley lamproites (Australia): Insights from melt and fluid inclusions. Gondwana Res 109:536–557. https://doi.org/10.1016/j.gr.2022.06.005

Akahama Y, Kawamura H (2006) Pressure calibration of diamond anvil Raman gauge to 310 GPa. J Appl Phys 100:043516. https://doi.org/10.1063/1.2335683

Akella A, Keszler DA (1995a) Crystal structure of the borate $Ba_2Ca(BO_3)_2$. Main Group Met Chem 18:35–42. https://doi.org/10.1515/mgmc.1995.18.1.35

Akella A, Keszler DA (1995b) Structure and Eu^{2+} luminescence of dibarium magnesium orthoborate. Mater Res Bull 30:105–111. https://doi.org/10.1016/0025-5408(94)00113-8

Arefiev AV, Shatskiy A, Podborodnikov IV, Rashchenko SV, Chanyshev AD, Litasov KD (2019) The system K_2CO_3–$CaCO_3$ at 3 GPa: link between phase relations and variety of K–Ca double carbonates at ≤ 0.1 and 6 GPa. Phys Chem Miner 46:229–244. https://doi.org/10/gncqwk

Arefiev AV, Shatskiy A, Podborodnikov IV, Litasov KD (2018) Melting and subsolidus phase relations in the system K_2CO_3–$MgCO_3$ at 3 GPa. High Pressure Res 38:422–439. https://doi.org/10/gncqwj

Bayarjargal L, Fruhner C-J, Schrodt N, Winkler B (2018) $CaCO_3$ phase diagram studied with Raman spectroscopy at pressures up to 50 GPa and high temperatures and DFT modeling. Phys Earth Planet In 281:31–45. https://doi.org/10.1016/j.pepi.2018.05.002

Bermanec V, Scholz R, Markovic F, Gobac Ž, Chaves M (2011) Mineralogy of the Boa Vista pegmatite, Galileia, Minas Gerais, Brazil. In: 5th International Symposium on Granitic Pegmatites, Mendoza, Argentina. pp 33–35

616 Birch F (1978) Finite strain isotherm and velocities for single-crystal and polycrystalline NaCl at
617 high pressures and 300°K. J Geophys Res 83:1257. https://doi.org/10.1029/JB083iB03p01257
618 Brey GP, Bulatov VK, Girnis AV (2011) Melting of K-rich carbonated peridotite at 6–10 GPa and
619 the stability of K-phases in the upper mantle. Chem Geol 281:333–342.
620 https://doi.org/10.1016/j.chemgeo.2010.12.019
621 Bruker (2016). APEX3. Madison, Wisconsin: Bruker AXS Inc.
622 Caracas R, Bobocioiu E (2011) The WURM project–a freely available web-based repository of
623 computed physical data for minerals. Am Mineral 96:437–443.
624 https://doi.org/10.2138/am.2011.3532
625 Chariton S, Cerantola V, Ismailova L, Bykova E, Bykov M, Kupenko I, McCammon C,
626 Dubrovinsky L (2017) The high-pressure behavior of spherocobaltite ($CoCO_3$): a single
627 crystal Raman spectroscopy and XRD study. Phys Chem Miner.
628 https://doi.org/10.1007/s0026 9-017-0902-5
629 Chayka IF, Kamenetsky VS, Vladykin NV, Kontonikas-Charos A, Prokopyev IR, Stepanov SY,
630 Krasheninnikov SP (2021) Origin of alkali-rich volcanic and alkali-poor intrusive carbonatites
631 from a common parental magma. Sci Rep 14. https://doi.org/10.1038/s41598-021-97014-y
632 Decius JC (1955) Coupling of the out-of-plane bending mode in nitrates and carbonates of the
633 aragonite structure. J Chem Phys 23:1290–1294. https://doi.org/10.1063/1.1742260
634 Efthimiopoulos I, Müller J, Winkler B, Ozten C, Harms M, Schade U, Koch-Müller M (2019)
635 Vibrational response of strontianite at high pressures and high temperatures and construction
636 of P–T phase diagram. Phys Chem Miner 46:27–35. https://doi.org/10.1007/s00269-018-
637 0984-8

638 Gillet P, Biellmann C, Reynard B, McMillan P (1993) Raman spectroscopic studies of carbonates
639 part I: High-pressure and high-temperature behaviour of calcite, magnesite, dolomite and
640 aragonite. Phys Chem Miner 20:1–18. https://doi.org/10.1007/BF00202245
641 Golubkova A, Merlini M, Schmidt MW (2015) Crystal structure, high-pressure, and high-
642 temperature behavior of carbonates in the $K_2Mg(CO_3)_2$–$Na_2Mg(CO_3)_2$ join. Am Mineral
643 100:2458–2467. https://doi.org/10/f72dmt
644 Harlow GE, Davies R (2004) Status report on stability of K-rich phases at mantle conditions.
645 Lithos 77:647–653. https://doi.org/10.1016/j.lithos.2004.04.010
646 Hou B, Huang S, Qin S (2022) Phase transitions and compressibility of alkali-bearing double
647 carbonates at high pressures: a first-principles calculations study. Phys Chem Miner 49:34.
648 https://doi.org/10.1007/s00269-022-01210-9
649 Jeanloz R (1981) Finite-strain equation of state for high-pressure phases. Geophys Res Lett
650 8:1219–1222. https://doi.org/10.1029/GL008i012p01219
651 Kraft S, Knittle E, Williams Q (1991) Carbonate stability in the Earth's mantle: A vibrational
652 spectroscopic study of aragonite and dolomite at high pressures and temperatures. J Geophys
653 Res 96:17997. https://doi.org/10.1029/91JB01749
654 Kresse G, Furthmüller J (1996) Efficient iterative schemes for *ab initio* total-energy calculations
655 using a plane-wave basis set. Phys Rev B 54:11169–11186.
656 https://doi.org/10.1103/PhysRevB.54.11169
657 Kunz M, Brown, ID (1995) Out-of-center distortions around octahedrally coordinated d0 transition
658 metals. J Sol State Chem 115: 395-406.

659 Lavina B, Dera P, Down RT, Yang W, Sinogeikin S, Meng Y, Shen G, Schiferl D (2010) Structure
660 of siderite $FeCO_3$ to 56 GPa and hysteresis of its spin-pairing transition. Phys Rev B
661 82:0641110
662 Logvinova AM, Shatskiy A, Wirth R, Tomilenko AA, Ugap'eva SS, Sobolev NV (2019)
663 Carbonatite melt in type Ia gem diamond. Lithos 342–343:463–467. https://doi.org/10/gjxnx6
664 Lv X, Wei L, Wang X, Xu J,Yu H, Hu Y, Zhang H, Zhang C, Wang J, Li Q (2018) Crystal growth,
665 electronic structure and optical properties of $Sr_2Mg(BO_3)_2$. J Solid State Chem 258:283–288.
666 https://doi.org/10.1016/j.jssc.2017.10.032
667 McKie D (1990) Subsolidus phase relations in the system $K_2Ca(CO_3)_2$–$Na_2Mg(CO_3)_2$ at 1 kbar; the
668 $fairchildite_{ss}$-buetschliite-eitelite eutectoid. Am Mineral 75:1147–1150
669 Meltzer A, Kessel R (2023) The metasomatism of sub-cratonic peridotites by a slab-derived fluid –
670 Implications for cratons' evolution. Geochim Cosmochim Acta 350:28–45.
671 https://doi.org/10.1016/j.gca.2023.03.034
672 Merlini M, Hanfland M, Gemmi M (2015) The $MnCO_3$-II high-pressure polymorph of
673 rhodochrosite. Am Mineral 100:2625–2629
674 Milton C, Axelrod J (1947) Fused wood-ash stones: fairchildite (n. sp.) $K_2CO_3 \cdot CaCO_3$, buetschliite
675 (n. sp.) $3K_2CO_3 \cdot 2CaCO_3 \cdot 6H_2O$ and calcite, $CaCO_3$, their essential components. Am Mineral
676 32:607–624
677 Momma K, Izumi F (2011) VESTA 3 for three-dimensional visualization of crystal, volumetric
678 and morphology data. J Appl Cryst 44:1272–1276.
679 https://doi.org/10.1107/S0021889811038970

680 Mrose ME, Rose HJ, Marinenko JW (1966) Synthesis and properties of fairchildite and
681 buetschliite: their relation to wood-ash stone formation. In: Program of the Geol Soc. Am.
682 Meeting, San Francisco
683 Pabst A (1974) Synthesis, properties, and structure of $K_2Ca(CO_3)_2$, buetschliite. Am Mineral 59:6
684 Palaich SE, Heffern RA, Hanfland M, Lausi A, Kavner A, Manning CE, Merlini M (2016) High-
685 pressure compressibility and thermal expansion of aragonite. Am Mineral 101: 1651-1658.
686 Peterson VK (2005) Lattice parameter measurement using Le Bail versus structural (Rietveld)
687 refinement: A caution for complex, low symmetry systems. Powder Diffr 20:14–17.
688 https://doi.org/10.1154/1.1810156
689 Rashchenko SV, Goryainov SV, Romanenko AV, Golovin AV, Korsakov AV, Moine Bn, Mikhno
690 AO (2017) High-pressure Raman study of nyerereite from Oldoinyo Lengai. J Raman
691 Spectrosc. 48:1438–1442. https://doi.org/10.1002/jrs.5152
692 Redfern SA, Angel RJ (1999). High-pressure behaviour and equation of state of calcite,
693 $CaCO_3$. Contrib Mineral Petr 134: 102–106.
694 Ross NL, Reeder RJ (1992). High-pressure structural study of dolomite and ankerite. Am
695 Mineral 77: 412–421.
696 Santamaria-Perez D, Pavic L, Chuliá-Jordán R, Ruiz-Fuertes J, Popescu C, Otero-de-la-Roza A
697 (2023) Phase stability of stress-sensitive Ag_2CO_3 silver carbonate at high pressures and
698 temperatures. Solid State Sci 135:107068.
699 https://doi.org/10.1016/j.solidstatesciences.2022.107068
700 Sawchuk K, Kamat R, McGuire C, Kavner A (2021) An X-ray diffraction and Raman
701 spectroscopic study of the high-pressure behavior of gaspéite ($Ni_{0.73}Mg_{0.27}CO_3$). Phys Chem
702 Miner 48:7. https://doi.org/10.1007/s00269-020-01133-3

703 Shannon RD (1976) Revised effective ionic radii and systematic studies of interatomic distances in
704 halides and chalcogenides. Acta Cryst A 32:751–767.
705 https://doi.org/10.1107/S0567739476001551
706 Shatskiy A, Borzdov YM, Litasov KD, Sharygin IS, Palyanov YN, Ohtani E (2015) Phase
707 relationships in the system K_2CO_3-$CaCO_3$ at 6 GPa and 900–1450°C. Am Mineral 100:223–
708 232. https://doi.org/10.2138/am-2015-5001
709 Sheldrick GM (2008) A short history of SHELX. Acta Cryst A
710 Shen G, Wang Y, Dewaele A, Wu C, Fratanduono DE, Eggert J, Klotz S, Dziubek KF, Loubeyre
711 P, Fat'yanov OV, Asimow PD, Mashimo T, Wentzcovitch RMM, et al (2020) Toward an
712 international practical pressure scale: A proposal for an IPPS ruby gauge (IPPS-Ruby2020).
713 High Pressure Res 40:299–314. https://doi.org/10/gmhp2z
714 Shimizu H (1985) Pressure-tuning resonance between the vibron and the libron in CH_2Br_2 and
715 CD_2Br_2 molecular solids. Phys Rev B 32:4120–4125. https://doi.org/10/bd8z5j
716 Tian H, Li Y, Zhang Q, Ningning S, Sun J, Xiao N, Liu Y, Zhang J, Liu H, Li Y (2023) Pressure-
717 dependent compressibility of $K_2X(CO_3)_2$ (X = Ca, Mg) under high pressure. Mater Lett
718 349:134895. https://doi.org/10.1016/j.matlet.2023.134895
719 Toby BH, Von Dreele RB (2013) GSAS-II: the genesis of a modern open-source all purpose
720 crystallography software package. J Appl Cryst 46:544–549.
721 https://doi.org/10.1107/S0021889813003531
722 Vennari CE, Beavers CM, Williams Q (2018) High-pressure/temperature behavior of the
723 alkali/calcium carbonate shortite ($Na_2Ca_2(CO_3)_3$): implications for carbon sequestration in
724 Earth's transition zone. J Geophys Res Solid Earth 123:6574–6591. https://doi.org/10/gj5n83

725 Vennari CE, Williams Q (2018) A novel carbon bonding environment in deep mantle high-
726 pressure dolomite. Am Mineral 103:171–174. https://doi.org/10/gc6m2n
727 Vennari CE, Williams Q (2019) High-pressure Raman and Nd^{3+} luminescence spectroscopy of
728 bastnäsite–(REE)CO_3F. Am Mineral 104:1389–1401. https://doi.org/10.2138/am-2019-7011
729 Wang M, Liu Q, Nie S, Li B, Wu Y, Gao J, Wei X, Wu X (2015) High-pressure phase transitions
730 and compressibilities of aragonite-structure carbonates: $SrCO_3$ and $BaCO_3$. Phys Chem Miner
731 42:517–527. https://doi.org/10.1007/s00269-015-0740-2
732 Wood RM, Palenik GJ (1999) Bond valence sums in coordination chemistry using new R_0 Values.
733 Potassium-oxygen complexes. Inorg Chem 38: 1031-1034
734 Yu-Feng Z, Jing L, Zhen-Xing Q, Chuan-Long L, Lun X, Rui L, LiGang B (2013) A high-pressure
735 study of $PbCO_3$ by XRD and Raman spectroscopy. Chin Phys C 37(3):038001.
736 https://doi.org/10.1088/1674-1137/37/3/038001
737 Zhang J, Martinez I, Guyot F, Gillet P, Saxena SK (1997) X-ray diffraction study of magnesite at
738 high pressure and high temperature. Phys Chem Miner 24:122–130.
739 https://doi.org/10.1007/s002690050025
740 Zhuravlev Yu N (2022) Vibration spectra of double K–Ca, K–Mg, and Na–Mg carbonates under
741 pressure. Geochem Int 60:1103–1113. https://doi.org/10.1134/S0016702922110118